Global and Planetary Change 221 (2023) 104049

Contents lists available at ScienceDirect

Global and Planetary Change

journal homepage: www.elsevier.com/locate/gloplacha

Neogene global climate change and East Asian dust sources: Combined rutile geochemistry and zircon U-Pb analysis from the northern Chinese Loess Plateau

Katja Bohm [a,b,*], Anu Kaakinen [a], Thomas Stevens [b], Yann Lahaye [c], Hugh O'Brien [c], Hui Tang [a,d,e], Yuan Shang [f], Hanzhi Zhang [g], Huayu Lu [g]

[a] Department of Geosciences and Geography, University of Helsinki, P.O. Box 64, 00014, Finland
[b] Department of Earth Sciences, Uppsala University, Villavägen 16, SE-752 36 Uppsala, Sweden
[c] Geological Survey of Finland, P.O. Box 96, 02151 Espoo, Finland.
[d] Finnish Meteorological Institute, Climate System Research, Helsinki, Finland
[e] Department of Geosciences, University of Oslo, Oslo, Norway
[f] State Key Laboratory of Estuarine and Coastal Research, East China Normal University, Shanghai 200241, China
[g] School of Geography and Ocean Science, Nanjing University, Nanjing, Jiangsu 210023, China

ARTICLE INFO

Editor: Howard Falcon-Lang

Original content: Detrital zircon U-Pb age and detrital rutile trace element data from the late Neogene Baode Red Clay sequence, Chinese Loess Plateau, and detrital rutile geochemistry from 14 potential source areas. (Original data)

Keywords:
Red clay
Late Cenozoic
Aeolian sediment
Multi-proxy single-grain provenance
East Asian winter monsoon
Westerly jet

ABSTRACT

During the late Neogene, global climate underwent a long-term transition to cooler climates that culminated in the Quaternary icehouse conditions. In the East Asian terrestrial realm, atmospheric dustiness increased, and the volume of aeolian dust deposits expanded significantly. The Neogene Red Clay deposits, located on the Chinese Loess Plateau (CLP), provide an exceptional geologic archive to investigate pre-Quaternary climates and environments. Constraining the provenance of the Red Clay is crucial for unravelling the links between late Neogene Central-East Asian climate, tectonics and desertification. However, Red Clay provenance is highly debated and data are scarce. In this study, we have used a multi-proxy approach at a high sampling resolution to study the provenance of the c. 7–2.6 Ma Baode Red Clay. Our data consist of joint detrital zircon U-Pb ages and detrital rutile trace element geochemistry of the Baode Red Clay, and of a massive rutile geochemistry dataset from 14 potential dust source areas. The data indicate that the Mio-Pliocene and Plio-Pleistocene global climate transitions were coupled with gradual dust provenance shifts. We propose these shifts indicate the intensification of East Asian winter monsoon and/or enhanced Central-East Asian drying as a response to global cooling. We also identify temporary Pliocene provenance changes that interrupt the long-term winter monsoon -controlled dust transport at c. 4 Ma and c. 3.5 Ma. Several indicators point to dust transport by the westerly jet at c. 4 Ma, possibly caused by a shift in the jet position as a response to global cooling, and/or enhanced wet deposition caused by intensified summer monsoon. Alternatively, the role of the paleo-Yellow River should be investigated further. We infer the 3.5 Ma provenance signal was caused by increased Yellow River -transported material from eroding Northeastern Tibetan Plateau and/or western CLP. Implications of our results not only shed light on the links between late Cenozoic global climate change and Central-East Asian dust cycle, but also provide detailed information to further investigate the late Neogene regional geomorphology and its effects on dust emission, transport, and deposition. Our combined rutile-zircon analysis also verifies that a multi-proxy single-grain approach that targets different types of primary source rocks is needed for reliable provenance analysis of the CLP dust.

1. Introduction

The Neogene-Quaternary boundary marks the transition of Earth's climate to full icehouse conditions. On the Chinese Loess Plateau (CLP), the area of aeolian Neogene Red Clay and Quaternary loess deposition greatly expanded over the last c. 8 Myr, potentially marking the impact

* Corresponding author at: Department of Geosciences and Geography, University of Helsinki, P.O. Box 64, 00014, Finland.
E-mail address: katja.bohm@helsinki.fi (K. Bohm).

https://doi.org/10.1016/j.gloplacha.2023.104049
Received 17 October 2022; Received in revised form 20 January 2023; Accepted 23 January 2023
Available online 31 January 2023

of one or a combination of global cooling, Tibetan Plateau (TP) uplift, and central-eastern Asian aridification on dust emission (e.g. Lu et al., 2010, 2019; Rea et al., 1998). While the Neogene-Quaternary climate transition is well marked on the CLP dust record by the change from Red Clay to loess deposits, debate exists over the possible provenance changes during the major global Mio-Pliocene and Plio-Pleistocene climate transitions. Based on CLP grain size variation (Wen et al., 2005), stepwise cooling first in the late Miocene (e.g. Herbert et al., 2016) and later in the mid-Pliocene (e.g. Fedorov et al., 2013) at least strengthened the dust-transporting winds (specifically the East Asian winter monsoon; EAWM), and/or expanded the dust source regions. However, without a detailed understanding on the dust provenance variation, further conclusions are limited.

Red Clay provenance work is hampered by several reasons. First, because the CLP receives material from multiple mixed sources, bulk sediment methods may not detect any provenance variation since c. 7 Ma (e.g. Bird et al., 2020). Second, the central CLP provenance signal may have been homogenized by reworked sediment (Licht et al., 2016). Third, the CLP dust record is strongly influenced by regional geological factors, such as TP uplift, Yellow River (YR) evolution, and East Asian summer monsoon (EASM) intensity, that may mask dust changes caused by global climate forcing (e.g. Nie et al., 2015). Moreover, the timing of late Neogene TP uplift events and YR formation are debated (e.g. An et al., 2001; Li et al., 2014; Pan et al., 2011; Zhang et al., 2021a). Ultimately, this lack of agreement prevents understanding of the major global to regional climatic and tectonic drivers of enhanced Neogene-Quaternary dustiness on the CLP.

Single-grain provenance techniques may be a solution to this impasse, as they allow tracing of sediment from multiple sources and via numerous recycling steps (e.g. von Eynatten and Dunkl, 2012; von Eynatten and Gaupp, 1999). However, even though single-grain zircon provenance work of Red Clay has increased over the past decade (e.g. Bohm et al., 2022; Nie et al., 2018; Shang et al., 2016; Sun et al., 2022; Zhang et al., 2018, 2022), ambiguities over the temporal provenance variation remain. This is partly explained by most studies using low-*N* analyses, using only one provenance proxy, or having low temporal sampling resolution. While an excellent provenance tracer on the CLP, zircons alone can be affected by fertility biases in source rocks, and cannot reveal many metamorphic source terranes (e.g. Bohm et al., 2022; Chew et al., 2020; Fenn et al., 2018; von Eynatten and Dunkl, 2012).

Here we address this through high-*N* detrital zircon U-Pb age analysis (N = 300–1000; Pullen et al., 2014) in combination with the first detailed application of detrital rutile trace element geochemistry as a provenance indicator (Bohm et al., 2022; Újvári et al., 2013) on the CLP dust deposits. To target the metamorphic primary sources, we present rutile data from the Baode Red Clay site and 14 potential source areas. Our multi-proxy dataset, incorporating previously published zircon U-Pb age data from northern CLP Red Clay (Shang et al., 2016; Sun et al., 2022), has high temporal resolution (mostly <0.5 Myr), which enables us to identify both longer-term gradual variation as well as geologically abrupt changes in Baode dust source(s) through the late Miocene to the end of Pliocene. As such, our large dataset reveals the nature and causes of changes in East Asian dustiness between c. 7.2–2.6 Ma in unprecedented detail.

2. Geological setting

Baode is located in Shanxi Province between the middle reaches of the YR and the Lüliang Mts. (Fig. 1). Located on the marginal northern CLP, the Baode Red Clay site is less likely fed by sediment derived from reworking of previous aeolian dust deposits than the southern or central CLP sites. Indeed, previous provenance work on the Baode Red Clay indicated its distinct provenance in comparison to southern and western CLP sites, and suggested mixed sources from the Central Asian Orogenic Belt (CAOB; Fig. 1) in the north/northwest and from the Northern Tibetan Plateau (NTP; Fig. 1) in the west (Shang et al., 2016).

Because of their richness in *Hipparion* fauna fossils, Zdansky (1923) named the Neogene deposits in Baode *Hipparion* Red Clay. Magnetostratigraphy of the Baode Red Clay constrained the deposition to

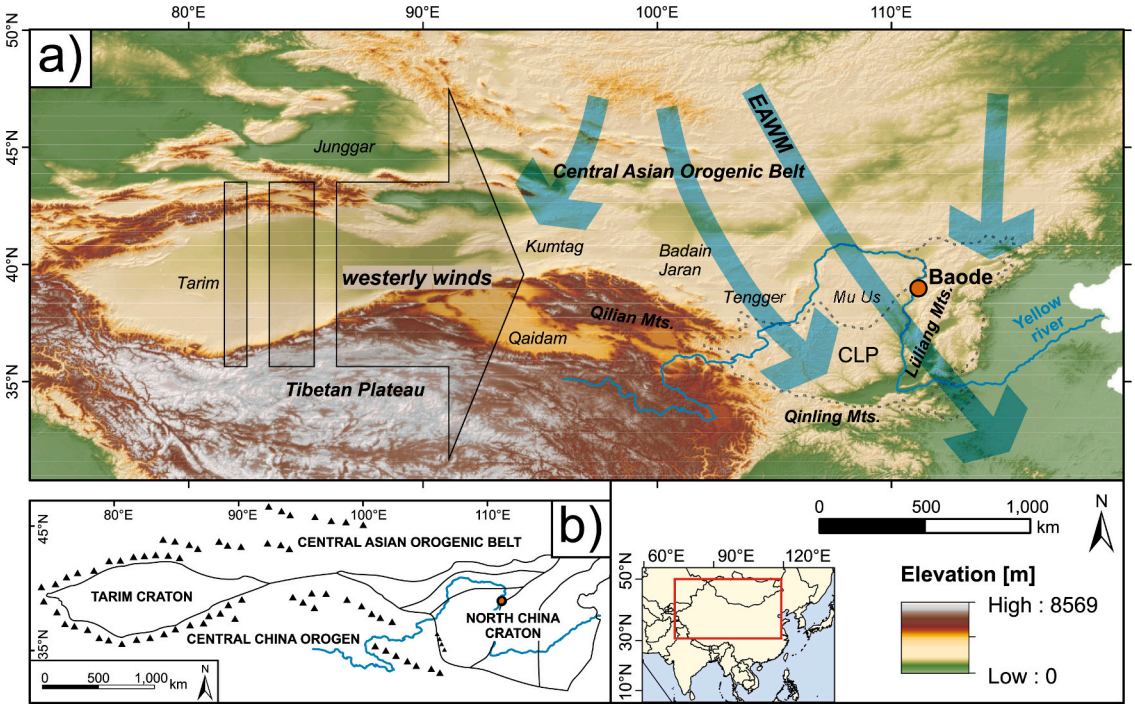

Fig. 1. a) Digital elevation model (Shuttle Radar Topography Mission) map and the approximate location of the Chinese Loess Plateau (CLP; dashed line), the Baode site, and potential source areas, and prevailing winds in the area of the Red Clay. EASM = East Asian summer monsoon. EAWM = East Asian winter monsoon. The term westerly winds here includes both the upper level jet stream (~200 hPa) and lower level westerly winds. b) Schematic map of the primary source regions discussed in the text. (For interpretation of the references to colour in this figure legend, the reader is referred to the web version of this article.)

7.23–2.72 Ma, following a transitional unit (TU) from Red Clay to Wucheng loess at 2.72–2.62 Ma (Zhu et al., 2008). In this paper, the TU is included when referring to Red Clay. The Baode Red Clay below the TU is divided into two formations (e.g. Zhu et al., 2008): the 7.23–5.34 Ma Baode Formation (BD) and the 5.34–2.72 Ma Jingle Formation (JL). The BD rests unconformably upon Paleozoic basement, and the lower part includes a fossil-free conglomerate bed, which in some localities is absent (Kaakinen et al., 2013; Zdansky, 1923). The sedimentary succession overlying the basal conglomerate is built up of 1–3 m thick sedimentary cycles of red-brown clayey silts and yellowish-brown silt capped by laterally continuous calcrete horizons. Infrequent conglomerate beds are interbedded within these fine-grained deposits (Kaakinen et al., 2013; Zhu et al., 2008). The JL, which rests conformably on the BD, is composed exclusively of fine grain sizes with a stronger rubification and more abundant Fe-Mn-coatings than the BD (Zhu et al., 2008). Two lithological units can be identified (boundary 3.6 Ma): the lower JL that has weaker soil development and less clay content and Fe-Mn coatings, and the upper JL which has the most strongly developed soils and abundant clay contents and Fe-Mn coatings (Zhu et al., 2008). The median grain size of the BD and JL fluctuate between 7.0 and 55.1 μm and 7.3–12.4 μm, respectively (Shang et al., 2016). On top of the TU, in which the colour of the sediment gradually changes upwards from reddish to yellow, lies Quaternary loess.

3. Materials and methods

3.1. Samples

The Red Clay samples for zircon and rutile analyses in this study include one TU, six JL (five with rutile data), and five BD samples (three with rutile data; Table 1). The BD samples and two of the JL samples (5.24 Ma and 3.5 Ma) have existing zircon data from Shang et al. (2016) (Table 1). Four new samples were collected from the JL and one from the TU from the Tanyugou profile in Baode area (38°53′36.9″N 111°08′49.0″E). The ages of these units were constrained to 4.04–2.64 Ma after Zhu et al. (2008). A sample summary is given in Table 1.

The source area samples (Table A1) for detrital rutile trace element analyses were collected from 14 selected areas to the west and northwest of the CLP. Heavy mineral composition, Sr, Nd and Hf isotopic composition, and/or detrital zircon U-Pb analyses from some of these samples have been previously published by Stevens et al. (2013), Rittner et al. (2016), and Bird et al. (2020).

3.2. Sample preparation

The rutiles and zircons of the new 4.04–2.64 Ma JL and TU samples, and the rutiles of the source area samples (excluding samples TGR, QDM and MD-9), were separated by diiodomethane heavy liquids (density 2.86/2.89 and 3.31 g m^{-3}) and Franz magnetic separator at the Mineral Separation Laboratory of Vrije Universiteit Amsterdam. For samples TGR, QDM and MD-9, the minerals were separated by LST Fastfloat (hydrated sodium heteropolytungstates in water) heavy liquid (density 2.82 g m^{-3}) and Franz magnetic separator at Uppsala University, Department of Earth Sciences. Rutiles and zircons were hand-picked from a non- or low-magnetic heavy mineral separate under an optical microscope, taking care to minimise introduced bias on picked minerals (Tables 1 and A1). The source area rutiles were hand-picked from 20 to 120 or 20–500 μm fractions with a focus on the < ~60 μm grains, and the Red Clay rutiles and zircons from 30 to 90 μm fractions, enabling a laser spot size up to 25 μm for the analyses (Tables 1 and A1).

All picked rutiles and zircons were mounted onto epoxy buttons and polished. The grains were then examined using Scanning Electron Microscopy (SEM; JEOL JSM-5900-LV; 20 kV, 1 nA) at the Geological Survey of Finland (GTK) to ensure only rutiles and zircons were picked. From backscattered electron images, areas free of visible inclusions, zonings and cracks were chosen for further analyses.

The heavy mineral separation of the BD samples and the 5.24 Ma JL sample was done by Shang et al. (2016). To analyse the rutiles from these samples, the heavy mineral separates of the 30–60 μm grain size fractions were mounted in epoxy and polished. A field emission (FE) SEM JEOL JSM-7100F (20 kV, 1 nA) at GTK was used to automatically locate the rutiles among the other heavy minerals. It should be noted that the analysis numbers from these samples are low because the automated FE-SEM does not discriminate inclusion-bearing rutiles from the inclusion-free rutiles during automated rutile identification. Therefore, the majority of rutiles from the BD samples and 5.24 Ma JL sample hosted inclusions and were excluded from the final data. To improve the statistics on these samples, additional rutiles were picked from the 60–90 μm non- or low-magnetic heavy fractions (Table 1).

3.3. Zircon U-Pb dating

To produce a high-*N* dataset of detrital zircon U-Pb ages, we analysed ~300 grains per sample, of which 228–255 grains gave concordant zircon ages with ±10% discordance limits. These limits are similar to those used in much previously published zircon data from Baode and source areas (e.g. Shang et al., 2016; Stevens et al., 2013). For better comparability, where needed, other published source area data (Appendix B) were reprocessed according to these limits. Zircon U-Pb analyses followed the same procedure as in Bohm et al. (2022). The analyses were conducted at GTK using a Nu Plasma AttoM single collector ICP-MS (Nu Instruments Ltd., Wrexham, UK) connected to an Analyte Excite 193 ArF laser ablation system (Photon Machines, San Diego, USA). The laser spot size was 25 μm, pulse frequency 5 Hz, and the beam energy density 2.5 J cm^{-2}. A threshold of 1 Ga was used for the $^{206}Pb/^{238}U$ (<1 Ga) and $^{207}Pb/^{206}Pb$ (> 1 Ga) concordant ages.

3.4. Rutile trace elements

The rutile trace element analysis by LA-ICP-MS follows Bohm et al.

Table 1
Baode Red Clay samples from this study and from Shang et al. (2016), and preparation of the samples analysed in this study. TU = transitional unit. JL = Jingle Formation. BD = Baode Formation. Zr = zircon U-Pb analysis. Rt = rutile trace element analysis.

Sample ID	Depositional unit	Age (Ma)	Locality	This study	Shang et al. (2016)	Rutile method (this study)
CH11–03-02	TU (JL-Loess)	2.64	Tanyugou	Zr + Rt	–	Picking from 30 to 90 μm
CH11–03-03	JL	2.79	Tanyugou	Zr + Rt	–	Picking from 30 to 90 μm
CH11–03-04	JL	3.39	Tanyugou	Zr + Rt	–	Picking from 30 to 90 μm
JL-2	JL	3.5	Yangjiagou	–	Zr	–
CH11–03-05	JL	3.67	Tanyugou	Zr + Rt	–	Picking from 30 to 90 μm
CH11–03-06	JL	4.04	Tanyugou	Zr + Rt	–	Picking from 30 to 90 μm
JL-1	JL	5.24	Yangjiagou	Rt	Zr	FE-SEM (30–60 μm) & picking (60–90 μm)
BD-5	BD	5.75	Daijiagou	Rt	Zr	FE-SEM (30–60 μm) & picking (60–90 μm)
BD-4	BD	6.19	Daijiagou	–	Zr	–
BD-3	BD	6.56	Daijiagou	Rt	Zr	FE-SEM (30–60 μm) & picking (60–90 μm)
BD-2	BD	6.91	Daijiagou	Rt	Zr	FE-SEM (30–60 μm) & picking (60–90 μm)
BD-1	BD	7.16	Daijiagou	–	Zr	–

(2022), using a spot size of 20 or 25 μm, depending on the grain size. Approximately 30–40% of the Red Clay rutile analyses were conducted with a 20 μm spot, while all the source area rutiles were analysed with a 25 μm spot. The analyses of the 30–60 μm grain size fractions of the BD samples and the 5.24 Ma JL sample were exceptionally run with a 4 mJ pulse energy at 30% attenuation, an energy flux of 2.0 J cm^{-2}, and a laser spot diameter of 15 μm. The time-resolved spectra were carefully studied in order to avoid the integration of mineral inclusions (sharp peaks) or cracks (unstable signal). When the signal window selection was not possible, the analysis was removed from the dataset.

Prior to further interpretations, rutiles were identified from the other TiO_2 polymorphs anatase and brookite by using the concentrations of Nb, Cr, Sn, Fe, V, and Zr (Triebold et al., 2011). Discrimination between metamafic and metapelitic rutiles using Cr and Nb contents followed Triebold et al. (2012). Zr-in-rutile temperatures were calculated after Tomkins et al. (2007) with a 10 kbar and α-quartz setting using the equation

$$T(^{\circ}C) = \frac{83.9 + 0.410P}{0.1428 - Rln[Zr(\text{ppm})]} - 273$$

where P is pressure in kbar and R is the gas constant, 0.0083144 kj K^{-1}. The uncertainty of the Zr-in-rutile temperature estimates, ultimately deriving from the analytical uncertainty of Zr concentration, is less than ±10 °C for most rutile grains that were measured with a laser spot diameter of 20–25 μm, and less than ±15 °C for most grains measured with a 15 μm spot. The uncertainty increases with higher Zr contents/temperatures.

3.5. Data visualisation and statistical analysis

The Kernel Density Estimates (KDEs) and the multivariate statistical analyses were made by using the R package 'provenance' (Vermeesch et al., 2016). First, separate Kolmogorov-Smirnov -based non-metric multidimensional scaling (MDS) maps (Vermeesch, 2013) were produced of the zircon ages, Zr-in-rutile temperatures, and source rock Cr-Nb discrimination values.

Next, Individual Differences Scaling (INDSCAL; Vermeesch and Garzanti, 2015) was used to combine the multi-proxy provenance data from the individual MDS configurations. INDSCAL transforms the MDS dissimilarity matrices from each individual MDS to a shared 'group configuration' by assigning different weights to the different provenance proxy datasets (Vermeesch and Garzanti, 2015). INDSCAL produces two plots: a 'group configuration', which illustrates the relative (dis-)similarities between samples, and a plot of 'source weights', which quantifies the relative importance of the different provenance proxies (Vermeesch and Garzanti, 2015; Vermeesch et al., 2016). A detailed description of the INDSCAL method for provenance research is found in e.g. Vermeesch and Garzanti (2015).

4. Results

4.1. New detrital zircon U-Pb age data of the 4.04–2.64 Ma JL-TU

The new zircon age data for the 4.04–2.64 Ma Red Clay samples are relatively uniform, with the highest age peak at 300–200 Ma, and a smaller peak at 500–400 Ma (Fig. 2). Smaller clusters of ages occur at c. 1000–500 Ma, 2000–1700 Ma, and c. 2500 Ma. The 2.64 Ma TU, and the 2.79 Ma, 3.67 Ma, and 4.04 Ma JL units also have multiple ages <200 Ma. Compared to other samples, the 4.04 Ma unit has a high proportion of 250–200 Ma ages and a very low proportion of Mesoproterozoic zircons. The 4.04–3.67 Ma units have higher proportions of 450–400 Ma ages than 500–450 Ma ages, while the opposite is true for the 3.39–2.64 Ma units. The 4.04–3.67 Ma units also have low amounts of 541–500 Ma ages compared to the 3.39–2.64 Ma units. In the 2.64 Ma TU, the Precambrian zircon proportion is the highest and the 400–300 Ma age proportion increases compared to the previous unit (Fig. 2).

4.2. Detrital rutile trace elements

The main diagnostic feature of provenance from the detrital rutile trace element geochemistry is the Zr-in-rutile metamorphic temperature. For clarity, in plotting the data we divide the amphibolite facies temperatures into lower (500–600 °C) and higher temperatures (600–750 °C), and distinguish the high temperature (HT; 800–900 °C) and ultra-high temperature (UHT; >900 °C) granulites from the lower granulite facies (750–800 °C). A more complete report of the rutile results is provided in Appendices A3–A5. It should be kept in mind that the rutile data of the BD samples and the JL 5.24 Ma sample consist mostly of coarser grain sizes (60–90 μm: Fig. A2).

Most Red Clay units yield 21–42% granulitic rutiles with median temperatures in the range of 660–725 °C, except the 4.04 Ma unit with only 13% granulitic rutiles and a median temperature of 636 °C, and the TU with 67% granulite facies rutiles and a median temperature of 832 °C (Fig. 2–4).

Of the source regions, the Ordos Block Cretaceous sandstone and the East Mu Us modern dune sand samples have the highest proportions of granulitic rutiles (62% and 41%, respectively), whereas Junggar modern sand stands out by having 95% amphibolite facies rutiles, no HT/UHT rutiles, and the lowest median temperature at 636 °C. The Cretaceous sandstone is the only source area sample with a granulite facies median temperature (773 °C; Fig. 3). Other source areas, except the East Mu Us (724 °C), have median temperatures in the amphibolite facies, mostly between 673 and 701 °C.

All the samples have dominant metapelitic source rock lithology according to the Cr-Nb discrimination (Figs. 2 & 4). Most source area samples have 2–9% metamafic rutiles. Exceptions are Junggar (20% mafic), Tarim (10%), and Ulanbuh (13%) modern sand samples. Most Red Clay units have 9–12% metamafic rutiles, except the 6.56 Ma (6%) and 3.39 Ma (18%) units (Fig. 2). Exceptionally high Cr-Nb values (> 200,000) are present in the NE Tengger, W Mu Us, and BD 6.56 Ma samples.

4.3. Multivariate statistical analyses

4.3.1. Detrital zircon U-Pb ages

The MDS plot (stress 8.3%) of the new and previously published (Shang et al., 2016) zircon ages of the Baode Red Clay and previously published source area data (Appendix B) positions the oldest, 7.16 Ma Red Clay unit closest to the Liupan Mts. detritus (Fig. 5a). The 6.91–5.75 Ma BD and the 3.5 Ma JL units are in one group that affiliates with the western sources from the Central China Orogen (CCO) detritus. The oldest (5.24 Ma) JL unit affiliates with the modern West Mu Us sands and the Upper YR sediments (Northeast TP). Another group of Red Clays are the 4.04–2.79 Ma JL units, of which the oldest sample plots slightly away from the other three units. The 3.67 Ma and 2.79 Ma JL units are closest to the modern Tengger Desert sands, while the 3.39 Ma unit is closest to the West Mu Us, and the 4.04 Ma unit is closest to the 3.67 Ma unit and second closest to the modern Kumtag Desert and Gobi sediments. The TU is distinct from the other Red Clay samples, with the closest affinity to the West North China Craton (NCC) and West Mu Us.

4.3.2. Detrital rutile trace elements

In the MDS map (stress 5.1%) of the Zr-in-rutile temperatures (Fig. 5b), most source areas plot close to each other because there is little variation in temperature distributions of most areas (Fig. 3). However, similarly to the zircon data, the upper YR samples (Dari and Zhenluo) and the West Mu Us plot close to each other, which is expected as the West Mu Us has been shown to receive material from the NTP via the YR (Stevens et al., 2013). Also, the Cretaceous sandstone and the East Mu Us are distinct from the West Mu Us for the same reason.

The 2.64 Ma TU and the 4.04 Ma JL units are distinct from the other

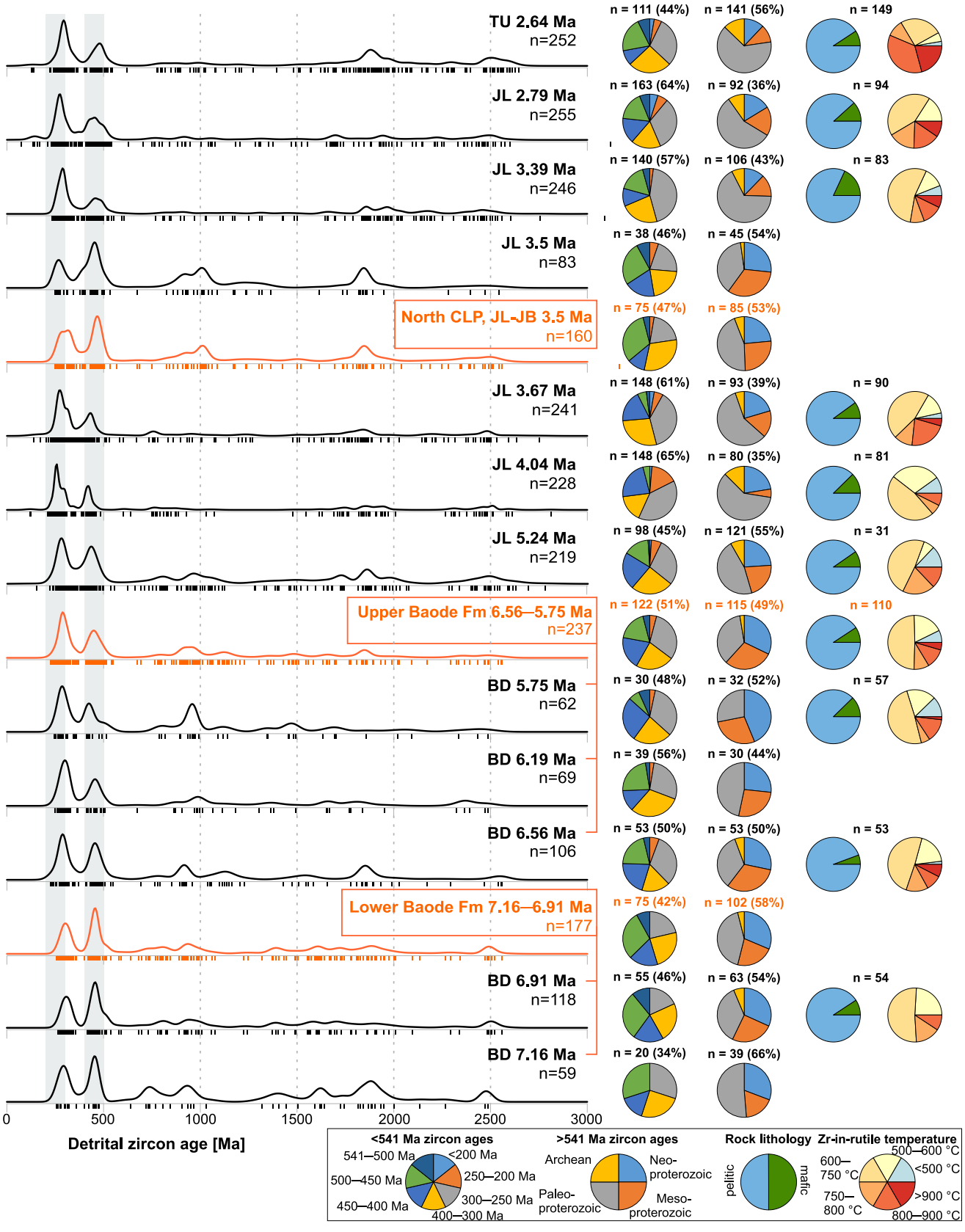

(caption on next page)

Fig. 2. The KDEs (adaptive bandwidth, except for the JL 3.5 Ma, BD 5.75 Ma, and BD 7.16 Ma samples with fixed 30 Myr bandwidth for better visual comparability with the other samples) and pie charts of the detrital zircon U-Pb ages, and pie charts of the rutile trace element data of the Baode Red Clay. The zircon age data of the 4.04–2.64 Ma units, excluding the 3.5 Ma unit, are from this paper. The zircon data of the 7.16–5.24 Ma and 3.5 Ma units are from Shang et al. (2016). Orange colour indicates a combination of multiple samples in order to increase the number of zircon analyses per sample; "Lower Baode Fm" is combined from the 7.16 and 6.91 Ma units, and "Upper Baode Fm" from the 6.56, 6.19, and 5.75 Ma units. To assess the reliability of the low-*N* data (Shang et al., 2016) of the 3.5 Ma JL unit, we have combined the 3.5 Ma JL zircon data with coeval northern CLP Red Clay data from the 3.5 Ma Jingbian (JB) Red Clay (Sun et al., 2022) as sample "North CLP, JL-JB 3.5 Ma". TU = Transitional Unit. JL = Jingle Formation. JB = Jingbian. BD = Baode Formation. Note the appearance of <250 Ma ages in the BD 6.56 Ma unit, and the increase in <300 Ma ages since 6.56 Ma. Most JL units have <200 Ma ages, unlike the BD units. Note the higher proportion of the 500–450 Ma ages over the 450–400 Ma ages in the Lower Baode Fm and since 3.5 Ma in the JL. A detailed version with the percentages of the pie charts is provided in Appendix A2. (For interpretation of the references to colour in this figure legend, the reader is referred to the web version of this article.)

Red Clay samples in the Zr-in-rutile temperature MDS map (Fig. 5b). Apart from these two exceptions, most of the Red Clay units plot near each other, and near the majority of the source areas. However, the BD samples are generally positioned more to the right side of the cluster, and the JL samples to the left side.

The MDS configuration (stress 8.0%) of the Cr-Nb source rock discrimination values (Fig. 5c) has more scatter than the other MDSs, possibly because of the larger range of the values (from −5974 to 351,489). The youngest samples (3.39–2.64 Ma) plot close to each other, but other temporal trends are not visible. Most source areas, except Junggar and Tarim, plot close to each other.

4.3.3. Combined datasets

The zircon ages and Zr-in-rutile temperatures were used in the INDSCAL group configuration. Because of the uncertainties of the Cr-Nb discrimination regarding exceptional geologic conditions (e.g. Triebold et al., 2012), and the high variability in the discrimination values, the lithology was not included in the INDSCAL plot (Appendix A4). In the INDSCAL map (Fig. 6), the BD units and the oldest JL unit plot close to each other, and closest to Qilian, Qaidam, Upper YR, and West Mu Us, while the 3.67–2.79 Ma JL units plot close to West Mu Us and Tengger. The 4.04 Ma unit and the TU are exceptional, mostly because of the rutile temperatures (*X*-direction). The INDSCAL map demonstrates how the small differences in the zircon ages (*Y*-direction) are more clearly visible in the rutile data (*X*-direction). The exceptional 4.04 Ma unit plots between Junggar and Tarim, and the TU is closest to Cretaceous sandstone of the source areas.

5. Discussion

5.1. Late Neogene environment and East Asian dust

Aeolian dust deposition expanded to the east of the Liupan Mts. at c. 8–7 Ma, concurrently with increased mass accumulation rates in the North Pacific (c. 8 Ma; Rea et al., 1998; Fig. 7c). A number of studies have inferred that aridification of the Asian interior (c. 8 Ma; An et al., 2001; Lu et al., 2010), EASM intensification (c. 8 Ma; An et al., 2001; Nie et al., 2018; Fig. 7b), and uplift of the northeastern TP (c. 8–7 Ma; Zheng et al., 2006 and references therein; Fig. 7b) and parts of the CAOB (c. 8–7 Ma; e.g. Dobretsov et al., 2016; Fig. 7b) all occurred at around this time. After the late Miocene global cooling (c. 7–5.4 Ma; Herbert et al., 2016; Fig. 7c), the early Pliocene climate warmed slightly (e.g. Fedorov et al., 2013), which, in Asia, coincided with EASM precipitation increases and possibly EAWM weakening, but continued central Asian drying (e.g. Ao et al., 2021). Dust flux to the North Pacific (ODP site 885/886) remained relatively low during c. 5.3–4 Ma, previously interpreted to indicate weaker westerly winds (Rea et al., 1998; Fig. 7c). The provenance of the central-southern CLP Red Clay does not show major variations through the Mio-Pliocene transition (Nie et al., 2018; Zhang et al., 2018; Fig. 7b). At c. 4 Ma, a long-term global cooling trend

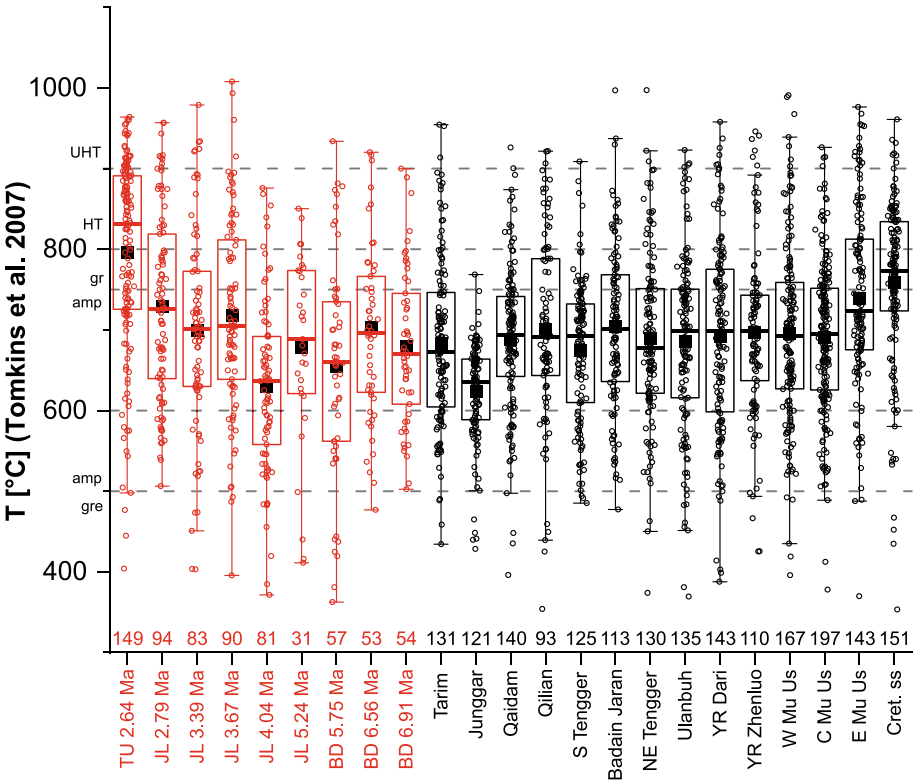

Fig. 3. Boxplots of Zr-in-rutile temperatures (Tomkins et al., 2007) of the Baode Red Clay and 14 potential source areas. The number of observations is shown below the plots. Data points are plotted as circles. The bold lines are median temperatures, and the squares mean temperatures. The boxes represent the upper and lower quartiles of the data. The whiskers represent ≤1.5 inter-quartile distance from the upper and lower quartiles. UHT = Ultra-high temperature. HT = high temperature. gr = granulite. amp = amphibolite. gre= greenschist. TU = transitional unit. JL = Jingle Formation. BD = Baode Formation. YR = Yellow River. (For interpretation of the references to colour in this figure legend, the reader is referred to the web version of this article.)

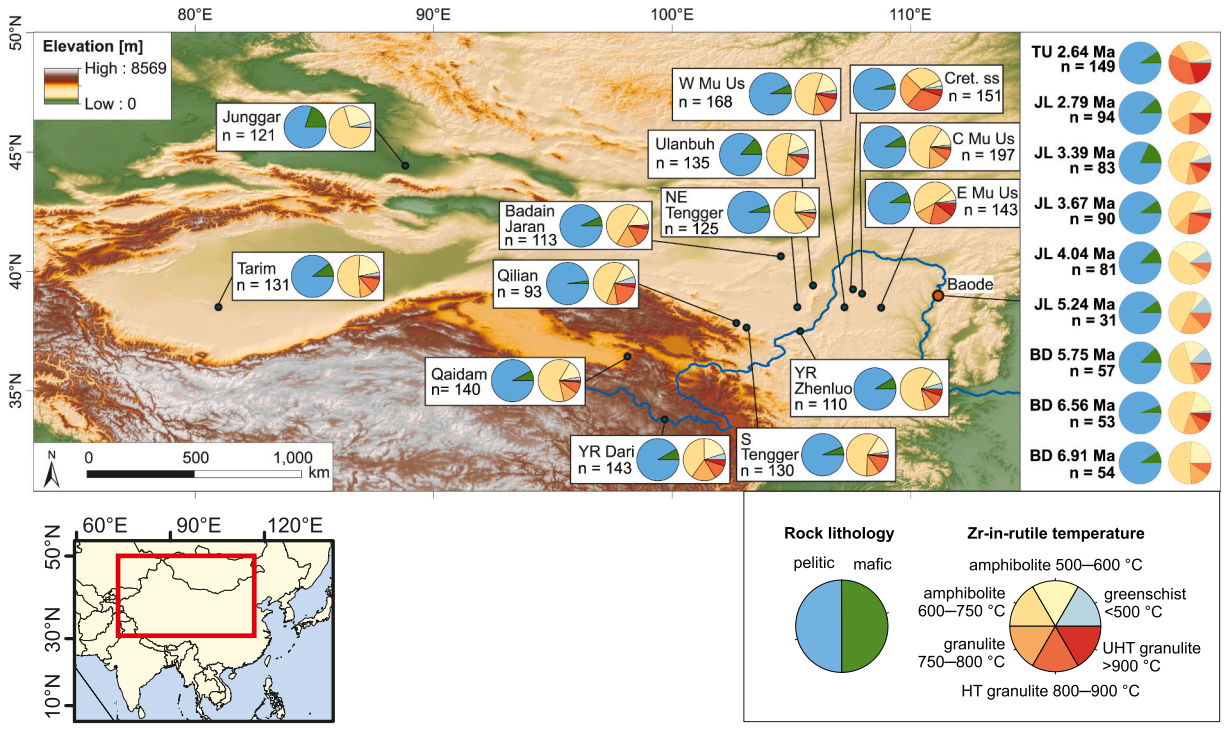

Fig. 4. Locations of the analysed samples in this study with their respective pie charts of Cr-Nb discrimination of rock lithology and Zr-in-rutile temperatures. TU = transitional unit. JL = Jingle Formation. BD = Baode Formation. YR = Yellow River. (For interpretation of the references to colour in this figure legend, the reader is referred to the web version of this article.)

started (e.g. Fedorov et al., 2013; Fig. 7c), which likely accelerated central Asian drying and/or strengthened the dust-transporting winds (Lu et al., 2010, 2019). The provenance of Chaona Red Clay (central CLP) slightly changed around this time, possibly caused by increased erosion in the proximal source areas due to intensified EASM (Nie et al., 2018; Fig. 7b). At c. 3.6 Ma, global climate became increasingly cold, intensifying the northern hemisphere glaciation (e.g. Mudelsee and Raymo, 2005) and the Siberian High -generated EAWM, as well as the westerly winds, indicated e.g. by the increased central Asian aridity and dust accumulation rates in the CLP and North Pacific (e.g. Lu et al., 2010; Rea et al., 1998; Fig. 7c). Furthermore, some evidence points to intensified EASM (An et al., 2001) and enhanced YR drainage at c. 3.7–3.6 Ma (Nie et al., 2015; Pan et al., 2011). However, in Baode, the climate became cooler and dryer at 3.5 Ma (Li et al., 2011). Despite these major changes in the global and regional climate and landscapes around 3.7–3.5 Ma, central or southern CLP Red Clay provenance did not seem to have any significant change around this time (Nie et al., 2018; Zhang et al., 2018). As the Quaternary began, the modern Gobi desert landscape formed (Lu et al., 2019), and provided more dust to southern CLP (Zhang et al., 2018). The YR influence on dust transport to the CLP was also notable during Quaternary (Nie et al., 2015; Stevens et al., 2013; Zhang et al., 2021b), but Neogene YR evolution remains ambiguous. Overall, despite these major climatic, landscape and environmental events, no clear link with Red Clay dust provenance changes has been agreed upon to date.

An illustration and a summary of the Baode Red Clay provenance inferences are presented in Fig. 8 and Table 2, respectively. We identify a gradual provenance shift from western to more northern-northwestern sources starting at c. 6.6 Ma, culminating in dominant dust transport by the EAWM in the Pliocene. This trend is consistent with long-term global cooling and its effects on central Asian drying and the EAWM intensity. However, two temporary provenance shifts also occurred in the Pliocene, at c. 4 Ma and 3.5 Ma. During these time intervals, the dust transport deviated from the long-term EAWM-dominated process. At the onset of Quaternary, the northern source contribution to Baode became even more pronounced than before.

5.2. *Gradual provenance shift from the late Miocene to Pliocene*

Overall, the BD and JL provenance is a mix of NTP (Qilian, Qaidam, Upper YR) and CAOB source materials (Fig. 5), in agreement with Shang et al. (2016). However, despite some uncertainty due to lower analysis number ($n = 177$) of the combined lower BD sample, the provenance of the upper and lower BD indicates some differences [compare 7.16–6.91 Ma (lower BD) and 6.56–5.75 Ma BD (upper BD) in Fig. 2]. The lower BD has a more pronounced NTP source signal, indicated by the more abundant 500–400 Ma ages. A stronger NTP signal could also derive from YR-transported NTP material (Stevens et al., 2013), but the formation time of the modern-type YR is highly debated (e.g. Liu, 2020; Nie et al., 2015; Wang et al., 2019; Zhang et al., 2021a). Instead, we suggest that the uplift of the northeastern TP at c. 8–7 Ma (Zheng et al., 2006 and references therein) controlled dust transport to Baode at c. 7 Ma by increasing silt generation in the NTP (e.g. Lu et al., 2022) and by lifting the dust near the westerly jet altitudes. This is consistent with the variation of magnetic susceptibility values across the CLP that also suggest an increased late Miocene NTP source contribution, especially to the western CLP (Wang et al., 2022).

The upper BD (c. 6.6–5.8 Ma) zircon age distribution, however, has the highest peak at 300–200 Ma, suggesting increased input from the CAOB sources or central deserts (Figs. 2 & 5d). The latter source is supported by the very high rutile Cr-Nb discrimination values (> 200,000) that are present only in the NE Tengger, W Mu Us, and BD 6.56 Ma samples. Furthermore, <250 Ma ages and a higher proportion of granulite-facies rutiles (albeit low-*N*) likely derive from northern proximal sources (Bohm et al., 2022). We infer that this trend towards increased northern/northwestern sources is part of a gradual shift in provenance related to the Mio-Pliocene transition, as discussed below.

The majority of the <5.24 Ma JL data plots separately from the BD samples in the MDS and INDSCAL maps, while the 5.24 Ma JL unit lies between them (Figs. 5a–b & 6). The BD samples affiliate with the NTP

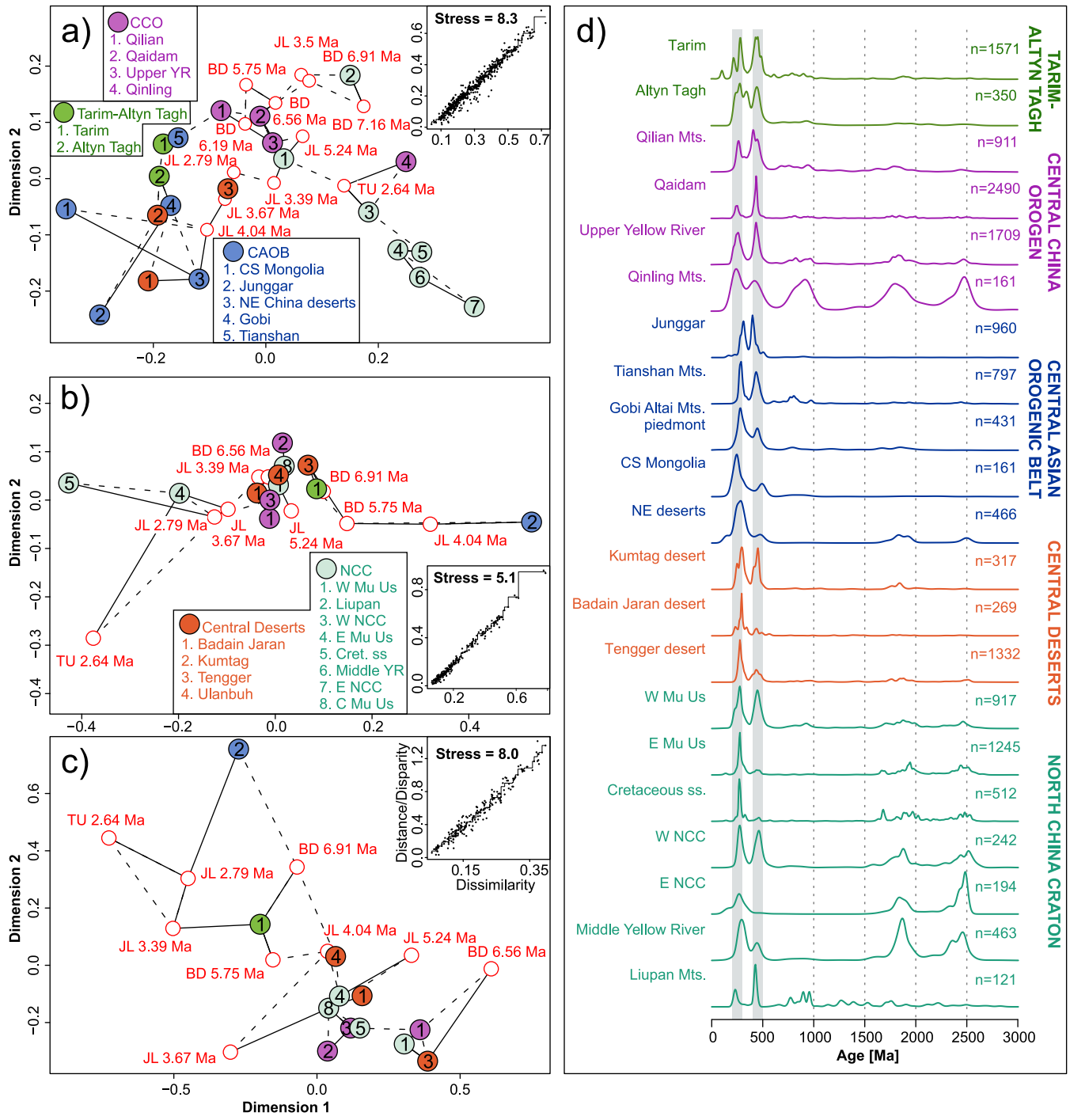

Fig. 5. MDS and Shepard plots for the Baode Red Clay and source area a) zircon U-Pb ages and b) Zr-in-rutile temperatures, and c) rutile Cr-Nb discrimination values after Triebold et al. (2012). The nearest (second nearest) neighbours in Kolmogorov-Smirnov space are indicated by solid (dashed) lines. d) Adaptive KDEs of the source area detrital zircon ages (data sources in Appendix B). TU = transitional unit. JL = Jingle Formation. BD = Baode Formation. CCO = Central China Orogen. CAOB = Central Asian Orogenic Belt. NCC = North China Craton. YR = Yellow River. Source region detrital zircon data sources and their locations are provided in Appendix B. (For interpretation of the references to colour in this figure legend, the reader is referred to the web version of this article.)

sources, and the JL samples generally plot closer to the central deserts, Mu Us, and CAOB in Figs. 5a–b & 6. The <5.24 Ma JL (except the 3.5 Ma) samples also have higher $n_{300–200\ Ma}/n_{500–400\ Ma}$ and $n_{Phanerozoic}/n_{Precambrian}$ ratios than the BD and 5.24 Ma JL (Fig. 7a) samples. Thus, dust provenance at Baode shifted from NTP sources in the late Miocene towards a more significant northwestern/northern CAOB source input (via the central deserts and Mu Us) in the Pliocene, coincident with the clearly observed lithologic change at the Mio-Pliocene transition. The Red Clay at Chaona, which mostly receives material from the NTP (Nie et al., 2018), has similar zircon age ratios as the BD (Fig. 7a–b), supporting our inferences.

Because the EAWM has operated since at least early Miocene (Guo et al., 2008), NTP uplift likely controlled the c. 7 Ma BD provenance signal. Subsequently, our data suggest that since c. 6.6 Ma, late Miocene cooling intensified the EAWM, which became the main carrier of dust, consistent with paleowind intensity indicators (Wen et al., 2005). Furthermore, a negative phase Arctic Oscillation -like (Mao et al., 2011) weaker late Pliocene westerly jet has been proposed from marine

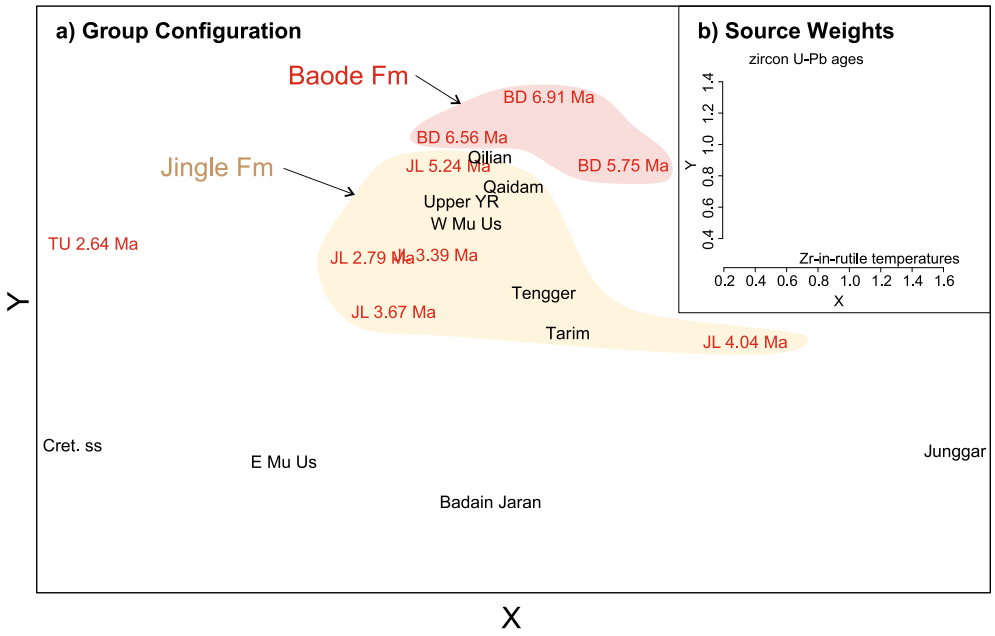

Fig. 6. An INDSCAL map [a) 'group configuration' -plot and b) 'source weights' -plot] combining detrital zircon U-Pb ages with detrital rutile metamorphic temperatures from the Baode Red Clay and ten potential source areas. The S and NE Tengger (= Tengger), as well as YR Dari and Zhenluo (= Upper YR) samples from the rutile dataset have been combined for comparison with the zircon data. The Ulanbuh and Central Mu Us rutile samples are excluded because of the lack of zircon U-Pb data from these areas. The map nicely illustrates the provenance transition between the BD and JL, leaving the oldest JL sample between the BD and most other JL samples. This transition is diagonal in the group configuration, indicating that both provenance proxies record the change. The exceptional samples (JL 4.04 Ma and TU 2.64 Ma) differ from the 3.67–2.79 Ma JL samples mainly in their Zr-in-rutile temperatures (*X*-axis), highlighting the importance of multi-proxy single-grain data. (For interpretation of the references to colour in this figure legend, the reader is referred to the web version of this article.)

records (Abell et al., 2021).

5.3. Abrupt provenance change at c. 4 Ma

The high proportions of low-temperature and mafic rutiles clearly point to a distinct provenance of the 4.04 Ma unit, supported by the zircon data (Figs. 2, 5, and 7a). The relatively abundant 250–200 Ma zircon ages of the 4.04 Ma unit could indicate northeastern primary sources linked to the Solonker suture (southeastern CAOB), a distal western primary source in West Kunlun (western CCO), or southern or southwestern primary sources in the CCO (Bohm et al., 2022). Northern/northeastern sources are unlikely, because HT/UHT rutiles and abundant Precambrian zircon ages from the proximal north/northeast would be expected (Bohm et al., 2022). Southwestern dust transporting winds unlikely existed in the Pliocene, but YR transport from southwest could be feasible (Nie et al., 2015; Stevens et al., 2013). A YR source, however, is inconsistent with the low proportion of 500–450 Ma ages, the high $n_{\text{Phanerozoic}}/n_{\text{Precambrian}}$ ratio, and the relatively high proportion of low-temperature and metamafic rutiles in the 4.04 Ma unit (Figs. 2, 4 & 7a). In the zircon age MDS map (Fig. 5a), the overall position of the 4.04 Ma unit is near the CAOB and central deserts. The closest source area is Kumtag Desert, which has abundant 250–200 Ma ages. The other above-mentioned features are consistent with the data from Junggar Basin, and some of them agree with Tarim, Ulanbuh, and Tengger zircon and/or rutile data (Figs. 5–7a).

In sum, a northerly transport trajectory and a proximal Mu Us source are improbable because of the lack of HT/UHT rutiles in the 4.04 Ma sample. The multiple provenance indicators of the 4.04 Ma unit point to material transported from the west from central deserts, Junggar and Tarim. The similarity of the 4.04 Ma unit to northerly CAOB sources could be explained by EAWM dust transport from Mongolia to the central deserts. Although not shown in our Qilian sample data, North Qilian consists of low-temperature metamorphic rocks, which, together with Tianshan and Tarim, form a zone of low-temperature western primary sources (Bohm et al., 2022), supporting the indicators of a western distal source for the 4.04 Ma unit. Additionally, tectonic activity in the Junggar Basin margins at c. 5 Ma (e.g. Dobretsov et al., 2016) may also have had an influence by increasing dust production in the area. Although the general view is that coarse silt is not feasible for long-distance aeolian transport, recent evidence suggests otherwise (van der Does et al., 2016). Furthermore, under the model of Wang et al. (2018), dust from the central deserts, and Tarim and Junggar Basins could have been lifted by the lower-level winds to the altitudes of the westerly jet, which could have in turn transported the dust to the CLP and North Pacific. Silt-sized dust from the upper troposphere is captured on the CLP mostly via wet deposition (Haugvaldstad, 2021). Thus the temporary nature of the c. 4.04 Ma provenance signal could be explained by a short-term summer monsoon intensification (Huang et al., 2007).

The westerly jet position is very sensitive to global temperature variations, both seasonally and on geologic timescales (Abell et al., 2021; Zhou et al., 2020; Mao et al., 2011). A southward shift in the position of the centre of the jet in reaction to the onset of long-term gradual global cooling at c. 4 Ma (e.g. Fedorov et al., 2013) could also explain the temporary nature of the 4.04 Ma provenance signal if the jet continued migrating after 4 Ma. A westerly jet -transport trajectory is supported by the increased dust flux at the ODP site 1208 at ca. 4 Ma (Fig. 7c; Abell et al., 2021), which, like Baode, lies at the centre of the modern day jet stream position over East Asia. Indeed, the more northern ODP site 885/886 does not show increased dust flux at 4 Ma (Fig. 7c).

Some uncertainties remain regarding the provenance of the 4.04 Ma unit. Because the North Qilian Mts. could be a primary source for the low-temperature rutiles of the 4.04 Ma unit (Bohm et al., 2022), and thermochronologic data suggest northeastern Qilian exhumed at c. 5 Ma (Wang et al., 2020), a paleo-YR transport from the eroding mountains could also partly explain the 4.04 Ma provenance signal. However, this scenario seems unlikely based on the existing detrital zircon and rutile data from Qilian, which are different to those of the 4.04 Ma unit (Figs. 5–7a). Future work targeting the c. 5.2–4.1 Ma Red Clay, lacking in our data, and a better understanding on the late Neogene YR system are crucial for reconstructing the dust cycle in northern CLP during the early Pliocene, and to verify our inferences on the 4.04 Ma JL provenance.

5.4. Abrupt provenance change at c. 3.5 Ma

Another temporary provenance shift occurs at 3.5 Ma, when the $n_{300\text{–}200\ \text{Ma}}/n_{500\text{–}400\ \text{Ma}}$ dipped below 1, contrary to all the other JL samples (Fig. 2). Although the number of zircons even in the combined North CLP JL-JB 3.5 Ma sample is too low for reliable quantitative provenance interpretations, the combined age distribution is very

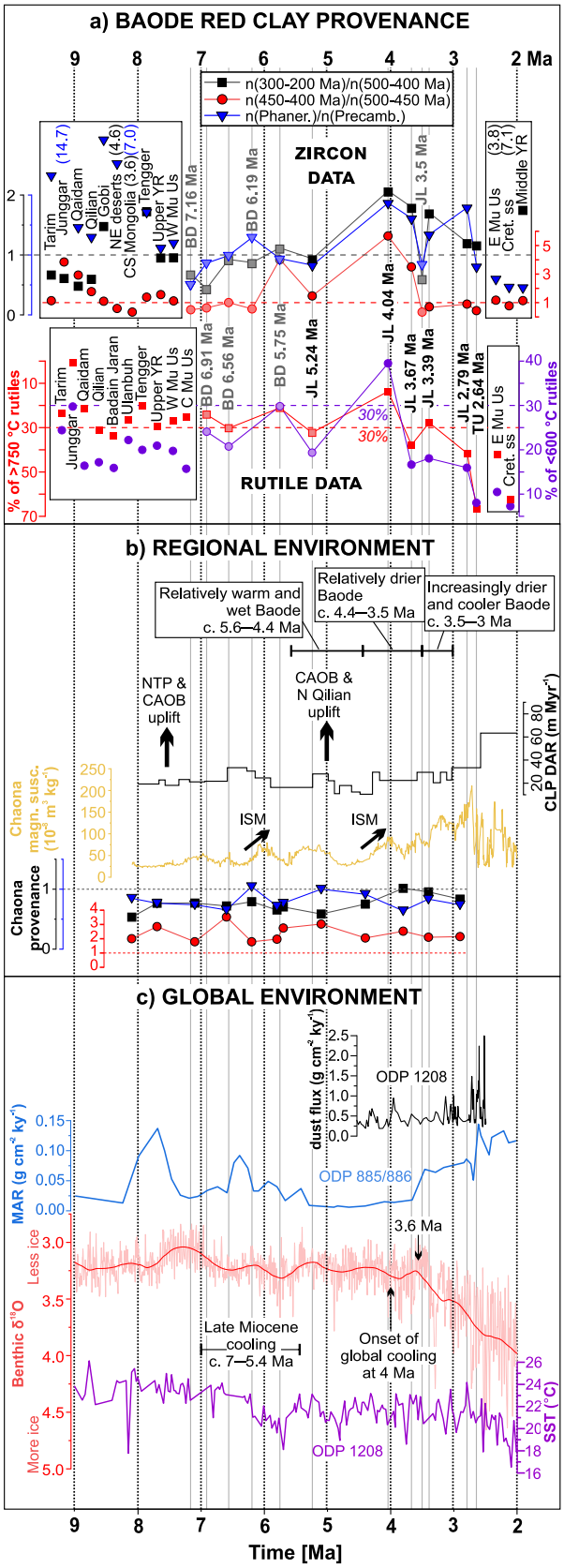

(caption on next column)

Fig. 7. Paleoclimate and -environment reconstructions compared with the provenance data of the Baode Red Clay. a) Baode Red Clay provenance data from this study, and previously published zircon data from the potential source areas (Appendix B). Written values in parenthesis refer to values outside the range of the plot. Blue colour of the text refers to the n(Phanerozoic)/n(Precambrian) value, and black colour to the n(300–200 Ma)/n(500–400 Ma) value. Note that the zircon and rutile data for low-*N* samples, indicated by the lighter colour of these data points, should be interpreted with caution. Note also the reversed axis of % of >750 °C rutiles. b) Regional environment from Baode and the CLP: Baode climate inferred from pollen data by Li et al. (2011); The Northern Tibetan Plateau (NTP), the Central Asian Orogenic Belt (CAOB), and NE Qilian uplift events referred to in the main text; dust accumulation rate in central CLP after Song et al. (2001) and Nie et al. (2018); magnetic susceptibility from Chaona (Song et al., 2001) and phases of intensified EASM (ISM) after Nie et al. (2018); detrital zircon U-Pb data from Chaona (Nie et al., 2018) (see legend in Fig. 7a, the scale of the axes is the same as in Fig. 7a); c) global climate indicators: dust flux at ODP site 1208 from Abell et al. (2021); dust mass accumulation rate at ODP site 885/886 from Rea et al. (1998); benthic oxygen isotopes from Westerhold et al. (2020), note the reversed axis; ODP site 1208 sea surface temperature (SST) from Herbert et al. (2016). (For interpretation of the references to colour in this figure legend, the reader is referred to the web version of this article.)

similar to that of the JL sample alone (Fig. 2). We therefore believe the low-*N* single-proxy data of the JL unit are reliable enough to infer provenance shifts. Importantly, these data point to significantly different dust sources at 3.5 Ma than before and after. This change is concurrent with multiple environmental, climatic, and tectonic events that could explain such a shift.

The 3.5 Ma JL provenance signal is strikingly similar to the lower BD units (Figs. 2, 5a, 7a). In contrast to our interpretation of the lower BD, we do not believe this provenance signal is caused by direct westerly aeolian transport from the NTP. Instead, we suggest the main source for the 3.5 Ma unit was YR-transported NTP and/or western CLP material to the West Mu Us, similar to the process described by Stevens et al. (2013), Nie et al. (2015) and Licht et al. (2016). Several indicators point to accelerated erosion of the NTP at c. 3.6 Ma (e.g. Li et al., 2014), and of the western CLP after c. 3.5 Ma (Zan et al., 2018), as well as to enhanced YR drainage at c. 3.7–3.6 Ma (Nie et al., 2015; Pan et al., 2011). Detrital zircon data of c. 5 Ma age Dongwan Red Clay from the western CLP are similar to those from the NTP (Shang et al., 2016). Additionally, enhanced YR drainage probably produced an increased local middle YR dust contribution to the 3.5 Ma JL (and JB) sample, indicated by the high proportion (54%) of Precambrian zircon ages (Figs. 2 & 7a). It should be noted that although some evidence points to an intensified EASM on the CLP at 3.6 Ma (An et al., 2001; Nie et al., 2018), the climate in Baode became significantly cooler and drier at 3.5 Ma (Fig. 7b; Li et al., 2011). Silt-sized particles from proximal source areas are mostly dry-deposited (Haugvaldstad, 2021), in agreement with the (possibly local) dry climate in Baode. This temporary change in dust transport mechanism, climatically and/or tectonically driven, was possibly undetected in Chaona (Nie et al., 2018) and Lantian (Zhang et al., 2018), where 3.6–3.5 Ma samples have not been analysed, and significant provenance changes between the 3.8/3.7 and 3.4 Ma units are not recorded. Furthermore, these sites already had a pronounced source component from the NTP, concealing the potentially increased NTP-signal from this shorter event. Moreover, the YR flowed northeastward before entering the Hetao Graben already in the Pliocene (e.g. Wang et al., 2019; Zhang et al., 2021a), thus transporting the NTP material closer to Baode and further from Chaona and Lantian. Global cooling -driven central Asian aridification at 3.6 Ma (e.g. Lu et al., 2010), likely also increased dust input from the CAOB sources to the 3.5 Ma JL-JB units. However, the provenance data suggest that this potential CAOB source, which was dominant throughout most the Pliocene (Section 5.2), is concealed by the stronger YR transport from the eroding NTP and/or western CLP. Recent detrital zircon U-Pb work reported high-*N* data from Red Clay at Jiaxian, on the North CLP, and quantified the relative contribution of the

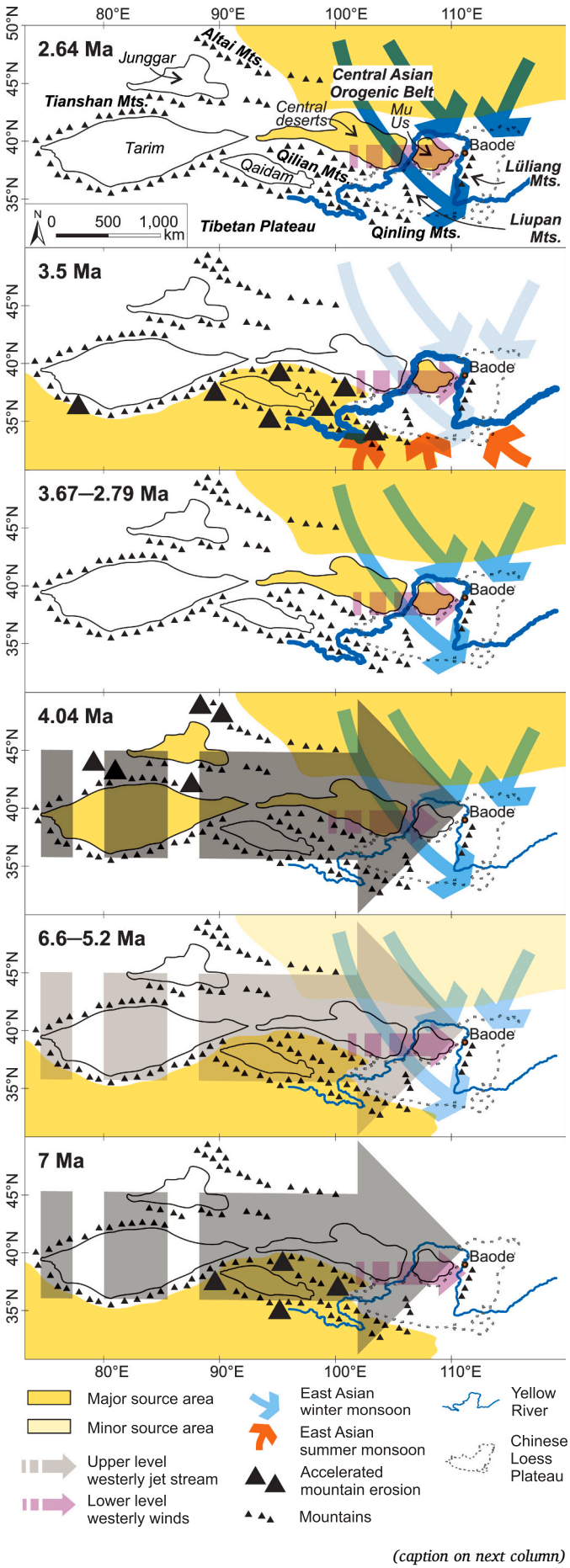

(caption on next column)

Fig. 8. A schematic figure illustrating the wind systems and source areas that are interpreted to have dominated the provenance signal in Baode Red Clay at each time interval discussed in the text. The regions are indicated in the topmost figure. The central deserts include the Kumtag, Badain Jaran, Tengger, and Ulanbuh deserts. The 3.67–2.79 Ma scene does not include the exceptional temporary provenance pattern at c. 3.5 Ma. A more intense shading of the arrows implies an increased importance of the corresponding wind to the provenance signal of Baode. A thicker Yellow River line refers to its higher importance as a sediment transporter to the northern CLP. Note that the Yellow River is presented at its modern day position, and the late Neogene river system was likely different than shown here. An alternative transport mechanism for the 4.04 Ma scene is mentioned in the text (Section 5.3). The absence of certain wind systems during certain time intervals in the figure does not indicate the absence of the wind system in question at the time, but that the wind system did not significantly contribute to the provenance signal in Baode.

Northeastern Qinghai-Tibetan Plateau sources as 42–54% during 3.7–3.4 Ma, which is a slight increase relative to values before and after (Zhang et al., 2022). However, according to the mutation tests performed by Zhang et al. (2022), there is no statistically significant change in the Northeastern Qinghai-Tibetan Plateau source contribution to Jiaxian during c. 8–2.6 Ma. As such, it currently remains unclear if the provenance shift shown at 3.5 Ma at Baode is a local or much wider event. More detrital zircons from the 3.5 Ma JL unit should be analysed, and from multiple sites preferably together with another provenance proxy, in order to test for the existence of the possible enhanced NTP erosional event and corresponding Red Clay source at the time.

5.5. Provenance variation in the mid-late Pliocene to Quaternary

In addition to the EAWM-controlled dust transport from the CAOB (Section 5.2), we find another, minor provenance trend in the Pliocene JL. Excluding the 3.5 Ma sample discussed above, the $n_{300–200\ Ma}/n_{500–400\ Ma}$, $n_{450–400\ Ma}/n_{500–450\ Ma}$, and $n_{Phanerozoic}/n_{Precambrian}$ ratios show decreasing linear trends from 4.04 to 2.64 Ma (Fig. 7a). We argue that these trends are partially controlled by a gradually increased proportion of YR-transported NTP material in the Yinchuan-Hetao graben system and/or West Mu Us, subsequently transported by the EAWM and low-level westerly wind to Baode, especially after the proposed 3.6–3.5 Ma YR-controlled dust event. This inference is consistent with the findings of Nie et al. (2015) and Wang et al. (2019).

The final clear provenance shift occurs at the Neogene-Quaternary transition. The 2.64 Ma TU has very high proportion of HT/UHT rutiles and Precambrian zircon ages (Fig. 2). Although the MDS map of zircon ages plots the Qinling Mts. close to the TU (Fig. 5a), we do not believe they are an important source for the unit, as southerly aeolian dust transport is unlikely, especially for the coarser grains (see also Section A3 regarding the grain size effect). The youngest JL unit (2.79 Ma) shows similarity to the TU, having increased proportions of granulitic rutiles and < 200 Ma zircon ages (see also Section A3). The HT/UHT rutiles likely derive from the proximal north, the <200 Ma zircon ages from proximal north/northeast, and the Precambrian zircons from the NCC (Bohm et al., 2022). Similar provenance signals are seen in the East Mu Us and Cretaceous sandstone, but in lesser proportions than in the TU, and the INDSCAL map implies that the main source region of the TU is not covered by the dataset (Fig. 6b). This could be explained by the poor coverage of northern source areas, such as southern Mongolia, in previously published detrital zircon (or rutile) data (Figs. 4 & B1). As the HT/UHT rutiles clearly point to northern source for the TU, we suggest a gradual shift, starting at c. 2.79 Ma, to the increasing dominance of EAWM dust transport in the Quaternary.

Previous zircon U-Pb provenance studies suggest an increased NTP dust input in early Quaternary loess to central CLP (Nie et al., 2018) and from the areas between the Gobi-Altay Mts. and NTP to the southern CLP (Zhang et al., 2018). Both of these studies point out changes in the

Table 2
A summary of the provenance interpretations discussed in detail in Section 5. NTP = Northern Tibetan Plateau. CAOB = Central Asian Orogenic Belt. EAWM = East Asian winter monsoon. YR = Yellow River. CLP = Chinese Loess Plateau. EASM = East Asian summer monsoon.

Time	Emission from	Main transport mechanism	Supporting paleoclimatic, paleoenvironmental, or modelling evidence
7 Ma	NTP	Westerly winds	N Pacific dust flux increase (Rea et al., 1998); Uplift of Northeastern TP (Zheng et al., 2006); Increased erosion in Qaidam Basin (e.g. Lu et al., 2022)
6.6–5.2 Ma	Increasing CAOB, minor NTP	Increasing EAWM, minor westerlies	Increasing aridity in central Asia (Ao et al., 2021; Lu et al., 2010); Relatively strong EAWM at c. 6.2–5.4 Ma (Wen et al., 2005); Late Miocene cooling (Herbert et al., 2016)
4 Ma	Central deserts (Kumtag, Badain Jaran, Tengger and Ulanbuh), possibly Junggar and Tarim Basins, possibly North Qilian	Westerly jet, paleo-YR?	Onset of long-term global cooling (Fedorov et al., 2013); Early Pliocene East Asia more wet, while central Asia more dry (e.g. Ao et al., 2021); Increased erosion at c. 5 Ma in Junggar Basin margins (Dobretsov et al., 2016); Wet deposition of silt-sized particles from the upper troposphere (Haugvaldstad, 2021); N Pacific dust flux increase at ODP site 1208 (Abell et al., 2021); Relatively weak northerly low-level wind (EAWM) at c. 5.4–3.5 Ma (Wen et al., 2005); Exhumation in NE Qilian at c. 5 Ma (Wang et al., 2020)
3.67–2.79 Ma	CAOB, central and Mu Us deserts	EAWM, YR + low-level westerly wind	Increasing aridity in central Asia and strengthening of the EAWM from c. 3.6–3.5 Ma onwards (Lu et al., 2010, 2019; Wen et al., 2005); Weaker late Pliocene westerly jet (Abell et al., 2021); YR evolution (see below)
3.5 Ma	NTP and/or Western CLP ➔ YR, W Mu Us	YR + low-level westerly wind, minor EAWM	Accelerated erosion of the NTP at c. 3.6 Ma (e.g. Li et al., 2014), and of the western CLP after c. 3.5 Ma (Zan et al., 2018); Enhanced YR drainage at c. 3.7–3.6 Ma (Nie et al., 2015; Pan et al., 2011); Intensified EASM on the CLP (An et al., 2001); Transition to drier and cooler climate in Baode (Li et al., 2011); Dry deposition of silt-sized particles from proximal areas (Haugvaldstad, 2021)
2.64 Ma	CAOB, primary sources to the north and northeast of Baode, central and Mu Us deserts	EAWM	Strengthening of EAWM (Wen et al., 2005); Further drying of central-eastern Asia (Lu et al., 2019); Onset of Quaternary icehouse conditions

source area dust production, and for the southern CLP, a stronger EAWM is also suggested. Our data may also indicate increased dust production via physical erosion in the mountains north of Baode towards the Quaternary. It is also evident that central-eastern Asian dry areas expanded at the onset of Quaternary (Lu et al., 2010, 2019). However, assuming a relatively stronger westerly jet after c. 2.73 Ma (Abell et al., 2021), without a relatively stronger EAWM, most of the dust from the northern and northeastern sources would have likely been blown directly to the east by the westerly winds without ever reaching Baode. In other words, even with increased dust production in northern source areas, a stronger EAWM is needed to transport this material.

6. Conclusions

In this paper, the provenance of the late Neogene aeolian Baode Red Clay was investigated through combined single-grain detrital zircon and rutile analyses. Baode dust provenance gradually responded to global paleoclimate changes at the Mio-Pliocene and Plio-Pleistocene transitions. The earliest Red Clay at c. 7 Ma was sourced mostly from the NTP, possibly as a response to tectonic forcing. Late Miocene cooling gradually increased the dust input from the northern/northwestern (CAOB) sources, and after the Mio-Pliocene boundary, dust was mostly transported from the central deserts, Mu Us, and CAOB, by the EAWM. However, at the onset of global cooling at c. 4 Ma, dust transport was possibly temporarily dominated by the upper level westerly jet from relatively distal sources, suggesting a shift in the jet position as a response to the climate change, and/or enhanced wet deposition caused by a temporarily intensified summer monsoon at 4 Ma. Alternatively, a possible contribution from the North Qilian Mts. via a paleo-YR should be investigated further. At c. 3.5 Ma, provenance data from the northern CLP indicate another temporary provenance shift. The main source at this time was possibly YR-transported material from the eroding NTP and/or western CLP, subsequently wind-transported to Baode by the EAWM and low-level westerlies. A minor mid-late Pliocene provenance trend of gradually increased YR-transported NTP-sediment in the proximal source areas of Baode is also observed. As global cooling towards the Quaternary icehouse proceeded, the northern source areas, and an EAWM transport, started to clearly dominate the Baode dust provenance.

The detrital rutile trace element data are consistent with zircon data, verifying the existence of these provenance changes in both metamorphic and igneous sources. Furthermore, the provenance changes at c. 4 Ma and 2.64 Ma are clearly observable in the rutile data, while zircon data only exhibit moderate differences. Gradual Mio-Pliocene provenance changes can be seen in both proxies. Our dataset demonstrates the need for two different but complementary mineral proxies in single-grain provenance studies to better identify potential source regions for the CLP dust.

Declaration of Competing Interest

The authors declare that they have no known competing financial interests or personal relationships that could have appeared to influence the work reported in this paper.

Data availability

Data for this study were published open access (Bohm et al., 2023).

Acknowledgements

We are grateful for Hilmar von Eynatten and an anonymous reviewer for their constructive comments and suggestions that helped to improve the manuscript substantially. Editor Jimin Sun is thanked for the editorial handling of the manuscript. KB gratefully acknowledges Roel

van Elsas (Vrije Universiteit Amsterdam) for helping with sample preparation. This research was supported by Magnus Ehrnrooth Foundation, Oskar Öflund Foundation, and GeoDoc grants to KB, Academy of Finland grants (316799 and 343602) to AK, a Swedish Research Council (2017-03888) grant and a STINT-NSFC mobility grant (CH2020-8688) to TS, NSFC (42021001 and 41920104005) grants to HL, and an NSFC (42001001) grant to YS.

Appendix. Supplementary data

Supplementary data to this article can be found online at https://doi.org/10.1016/j.gloplacha.2023.104049.

References

Abell, J.T., Winckler, G., Anderson, R.F., Herbert, T.D., 2021. Poleward and weakened westerlies during Pliocene warmth. Nature 589 (7840), 70–75.
An, Z., Kutzbach, J.E., Prell, W.L., Porter, S.C., 2001. Evolution of Asian monsoons and phased uplift of the Himalaya–Tibetan plateau since Late Miocene times. Nature 411, 62.
Ao, H., Rohling, E.J., Zhang, R., Roberts, A.P., Holbourn, A.E., Ladant, J.-B., Dupont-Nivet, G., Kuhnt, W., Zhang, P., Wu, F., Dekkers, M.J., Liu, Q., Liu, Z., Xu, Y., Poulsen, C.J., Licht, A., Sun, Q., Chiang, J.C.H., Liu, X., Wu, G., Ma, C., Zhou, W., Jin, Z., Li, X., Li, X., Peng, X., Qiang, X., An, Z., 2021. Global warming-induced Asian hydrological climate transition across the Miocene–Pliocene boundary. Nat. Commun. 12, 6935.
Bird, A., Millar, I., Rodenburg, T., Stevens, T., Rittner, M., Vermeesch, P., Lu, H., 2020. A constant Chinese Loess Plateau dust source since the late Miocene. Quat. Sci. Rev. 227, 106042.
Bohm, K., Stevens, T., Kaakinen, A., Lahaye, Y., O'Brien, H., Zhang, Z., 2022. The provenance of late Cenozoic East Asian Red Clay: Tectonic-metamorphic history of potential source regions and a novel combined zircon-rutile approach. Earth Sci. Rev. 225, 103909.
Bohm, Katja, Kaakinen, Anu, Stevens, Thomas, Lahaye, Yann, O'Brien, Hugh, Tang, Hui, Shang, Yuan, Zhang, Hanzhi, Lu, Huayu, 2023. Detrital zircon U-Pb age and detrital rutile trace element data from the late Neogene Baode Red Clay sequence, Chinese Loess Plateau, and detrital rutile geochemistry from 14 potential source areas. PANGAEA. https://doi.org/10.1594/PANGAEA.951048.
Chew, D., O'Sullivan, G., Caracciolo, L., Mark, C., Tyrrell, S., 2020. Sourcing the sand: accessory mineral fertility, analytical and other biases in detrital U-Pb provenance analysis. Earth Sci. Rev. 202, 103093.
Dobretsov, N.L., Buslov, M.M., Vasilevsky, A.N., Vetrov, E.V., Nevedrova, N.N., 2016. Cenozoic history of topography in southeastern Gorny Altai: thermochronology and resistivity and gravity records. Russ. Geol. Geophys. 57, 1525–1534.
van der Does, M., Korte, L.F., Munday, C.I., Brummer, G.J.A., Stuut, J.B.W., 2016. Particle size traces modern Saharan dust transport and deposition across the equatorial North Atlantic. Atmos. Chem. Phys. 16, 13697–13710.
von Eynatten, H., Dunkl, I., 2012. Assessing the sediment factory: the role of single grain analysis. Earth Sci. Rev. 115 (1), 97–120.
von Eynatten, H., Gaupp, R., 1999. Provenance of cretaceous synorogenic sandstones in the Eastern Alps: constraints from framework petrography, heavy mineral analysis and mineral chemistry. Sediment. Geol. 124 (1), 81–111.
Fedorov, A.V., Brierley, C.M., Lawrence, K.T., Liu, Z., Dekens, P.S., Ravelo, A.C., 2013. Patterns and mechanisms of early Pliocene warmth. Nature 496, 43–49.
Fenn, K., Stevens, T., Bird, A., Limonta, M., Rittner, M., Vermeesch, P., Andò, S., Garzanti, E., Lu, H., Zhang, H., Lin, Z., 2018. Insights into the provenance of the Chinese Loess Plateau from joint zircon U-Pb and garnet geochemical analysis of last glacial loess. Quat. Res. 89, 645–659.
Guo, Z.T., Sun, B., Zhang, Z.S., Peng, S.Z., Xiao, G.Q., Ge, J.Y., Hao, Q.Z., Qiao, Y.S., Liang, M.Y., Liu, J.F., Yin, Q.Z., Wei, J.J., 2008. A major reorganization of Asian climate by the early Miocene. Clim. Past 4, 153–174.
Haugvaldstad, O.W., 2021. Aeolian Dust Sources, Transport and Deposition over the Chinese Loess Plateau during 1999–2019: A Study Using the FLEXDUST and FLEXPART Models. Department of Geosciences. University of Oslo, p. 99.
Herbert, T.D., Lawrence, K.T., Tzanova, A., Peterson, L.C., Caballero-Gill, R., Kelly, C.S., 2016. Late Miocene global cooling and the rise of modern ecosystems. Nat. Geosci. 9, 843–847.
Huang, Y., Clemens, S.C., Liu, W., Wang, Y., Prell, W.L., 2007. Large-scale hydrological change drove the late Miocene C4 plant expansion in the Himalayan foreland and Arabian Peninsula. Geology 35, 531–534.
Kaakinen, A., Passey, H., Zhang, B., Liu, Z., Pesonen, J., Fortelius, M., 2013. Stratigraphy and Paleoecology of the Classical Dragon Bone Localities of Baode County, Shanxi Province. In: Wang, X., Flynn, L.J., Fortelius, M. (Eds.), Fossil Mammals of Asia: Neogene Biostratigraphy and Chronology. Columbia University Press, New York, pp. 203–217.
Li, J., Fang, X., Song, C., Pan, B., Ma, Y., Yan, M., 2014. Late Miocene–Quaternary rapid stepwise uplift of the NE Tibetan Plateau and its effects on climatic and environmental changes. Quat. Res. 81, 400–423.
Li, X., Fang, X., Wu, F., Miao, Y., 2011. Pollen evidence from Baode of the northern Loess Plateau of China and strong East Asian summer monsoons during the early Pliocene. Chin. Sci. Bull. 56, 64–69.
Licht, A., Pullen, A., Kapp, P., Abell, J., Giesler, N., 2016. Eolian cannibalism: Reworked loess and fluvial sediment as the main sources of the Chinese Loess Plateau. GSA Bull. 128, 944–956.
Liu, Y., 2020. Neogene fluvial sediments in the northern Jinshaan Gorge, China: Implications for early development of the Yellow River since 8 Ma and its response to rapid subsidence of the Weihe-Shanxi Graben. Palaeogeogr. Palaeoclimatol. Palaeoecol. 546, 109675.
Lu, H., Wang, X., Li, L., 2010. Aeolian sediment evidence that global cooling has driven late Cenozoic stepwise aridification in Central Asia. Geol. Soc. Lond., Spec. Publ. 342, 29–44.
Lu, H., Wang, X., Wang, X., Chang, X., Zhang, H., Xu, Z., Zhang, W., Wei, H., Zhang, X., Yi, S., Zhang, W., Feng, H., Wang, Y., Wang, Y., Han, Z., 2019. Formation and evolution of Gobi Desert in central and eastern Asia. Earth Sci. Rev. 194, 251–263.
Lu, H., Malusà, M.G., Zhang, Z., Guo, L., Shi, X., Ye, J., Sang, S., Xiong, S., Pan, J., Li, H., 2022. Syntectonic sediment recycling controls eolian deposition in Eastern Asia since ~8 Ma. Geophys. Res. Lett. 49 (3) e2021GL096789.
Mao, R., Ho, C.-H., Shao, Y., Gong, D.-Y., Kim, J., 2011. Influence of Arctic Oscillation on dust activity over Northeast Asia. Atmos. Environ. 45, 326–337.
Mudelsee, M., Raymo, M.E., 2005. Slow dynamics of the Northern Hemisphere glaciation. Paleoceanography 20 (4).
Nie, J., Stevens, T., Rittner, M., Stockli, D., Garzanti, E., Limonta, M., Bird, A., Andò, S., Vermeesch, P., Saylor, J., Lu, H., Breecker, D., Hu, X., Liu, S., Resentini, A., Vezzoli, G., Peng, W., Carter, A., Ji, S., Pan, B., 2015. Loess Plateau storage of Northeastern Tibetan Plateau-derived Yellow River sediment. Nat. Commun. 6, 8511.
Nie, J., Pullen, A., Garzione, C.N., Peng, W., Wang, Z., 2018. Pre-Quaternary decoupling between Asian aridification and high dust accumulation rates. Sci. Adv. 4, eaao6977.
Pan, B., Hu, Z., Wang, J., Vandenberghe, J., Hu, X., 2011. A magnetostratigraphic record of landscape development in the eastern Ordos Plateau, China: transition from late Miocene and early Pliocene stacked sedimentation to late Pliocene and Quaternary uplift and incision by the Yellow River. Geomorphology 125, 225–238.
Pullen, A., Ibáñez-Mejía, M., Gehrels, G.E., Ibáñez-Mejía, J.C., Pecha, M., 2014. What happens when n= 1000? Creating large-n geochronological datasets with LA-ICP-MS for geologic investigations. J. Anal. At. Spectrom. 29, 971–980.
Rea, D.K., Snoeckx, H., Joseph, L.H., 1998. Late Cenozoic Eolian deposition in the North Pacific: Asian drying, Tibetan uplift, and cooling of the northern hemisphere. Paleoceanography 13, 215–224.
Rittner, M., Vermeesch, P., Carter, A., Bird, A., Stevens, T., Garzanti, E., Andò, S., Vezzoli, G., Dutt, R., Xu, Z., Lu, H., 2016. The provenance of Taklamakan desert sand. Earth Planet. Sci. Lett. 437, 127–137.
Shang, Y., Beets, C.J., Tang, H., Prins, M.A., Lahaye, Y., van Elsas, R., Sukselainen, L., Kaakinen, A., 2016. Variations in the provenance of the late Neogene Red Clay deposits in northern China. Earth Planet. Sci. Lett. 439, 88–100.
Song, Y., Fang, X., Li, J., An, Z., Miao, X., 2001. The late Cenozoic uplift of the Liupan Shan, China. Sci. China Ser. D Earth Sci. 44, 176–184.
Stevens, T., Carter, A., Watson, T.P., Vermeesch, P., Andò, S., Bird, A.F., Lu, H., Garzanti, E., Cottam, M.A., Sevastjanova, I., 2013. Genetic linkage between the Yellow River, the Mu Us desert and the Chinese Loess Plateau. Quat. Sci. Rev. 78, 355–368.
Sun, J., Ding, Z., Xiao, W., Windley, B.F., 2022. Coupling between uplift of the Central Asian Orogenic Belt-NE Tibetan Plateau and accumulation of aeolian Red Clay in the inner Asia began at ~7 Ma. Earth Sci. Rev. 226, 103919.
Tomkins, H.S., Powell, R., Ellis, D.J., 2007. The pressure dependence of the zirconium-in-rutile thermometer. J. Metamorph. Geol. 25, 703–713.
Triebold, S., Luvizotto, G.L., Tolosana-Delgado, R., Zack, T., von Eynatten, H., 2011. Discrimination of TiO2 polymorphs in sedimentary and metamorphic rocks. Contrib. Mineral. Petrol. 161, 581–596.
Triebold, S., von Eynatten, H., Zack, T., 2012. A recipe for the use of rutile in sedimentary provenance analysis. Sediment. Geol. 282, 268–275.
Újvári, G., Klötzli, U., Kiraly, F., Ntaflos, T., 2013. Towards identifying the origin of metamorphic components in Austrian loess: insights from detrital rutile chemistry, thermometry and U–Pb geochronology. Quat. Sci. Rev. 75, 132–142.
Vermeesch, P., 2013. Multi-sample comparison of detrital age distributions. Chem. Geol. 341, 140–146.
Vermeesch, P., Garzanti, E., 2015. Making geological sense of 'Big Data' in sedimentary provenance analysis. Chem. Geol. 409, 20–27.
Vermeesch, P., Resentini, A., Garzanti, E., 2016. An R package for statistical provenance analysis. Sediment. Geol. 336, 14–25.
Wang, W., Zheng, D., Li, C., Wang, Y., Zhang, Z., Pang, J., Wang, Y., Yu, J., Wang, Y., Zheng, W., Zhang, H., Zhang, P., 2020. Cenozoic Exhumation of the Qilian Shan in the Northeastern Tibetan Plateau: evidence from low-temperature thermochronology. Tectonics 39 e2019TC005705.
Wang, X., Nie, J., Stevens, T., Zhang, H., Xiao, W., 2022. Resolving conflicting models of late Miocene East Asian summer monsoon intensity recorded in Red Clay deposits on the Chinese Loess Plateau. Earth Sci. Rev. 234, 104200.
Wang, Z., Nie, J., Wang, J., Zhang, H., Peng, W., Garzanti, E., Hu, X., Stevens, T., Pfaff, K., Pan, B., 2019. Testing Contrasting Models of the Formation of the Upper Yellow River using Heavy-Mineral Data from the Yinchuan Basin Drill Cores. Geophys. Res. Lett. 46, 10338–10345.
Wen, L., Lu, H., Qiang, X., 2005. Changes in grain-size and sedimentation rate of the Neogene Red Clay deposits along the Chinese Loess Plateau and implications for the palaeowind system. Sci. China Ser. D Earth Sci. 48, 1452–1462.
Westerhold, T., Marwan, N., Drury, A.J., Liebrand, D., Agnini, C., Anagnostou, E., Barnet, J.S.K., Bohaty, S.M., Vleeschouwer, D.D., Florindo, F., Frederichs, T., Hodell, D.A., Holbourn, A.E., Kroon, D., Lauretano, V., Littler, K., Lourens, L.J., Lyle, M., Pälike, H., Röhl, U., Tian, J., Wilkens, R.H., Wilson, P.A., Zachos, J.C.,

2020. An astronomically dated record of Earth's climate and its predictability over the last 66 million years. Science 369, 1383–1387.
Zan, J., Fang, X., Zhang, W., Yan, M., Zhang, D., 2018. A new record of late Pliocene-early Pleistocene aeolian loess–red clay deposits from the western Chinese Loess Plateau and its palaeoenvironmental implications. Quat. Sci. Rev. 186, 17–26.
Zdansky, O., 1923. Fundorte der Hipparion-Fauna um Pao-Te-Hsien in NW-Shansi. Bull. Geol. Surv. China 5, 69–82.
Zhang, H., Lu, H., Stevens, T., Feng, H., Fu, Y., Geng, J., Wang, H., 2018. Expansion of Dust Provenance and Aridification of Asia since ~7.2 Ma Revealed by Detrital Zircon U-Pb Dating. Geophys. Res. Lett. 45, 13,437-413,448.
Zhang, H., Lu, H., Zhou, Y., Cui, Y., He, J., Lv, H., Wang, K., Wang, X., 2021a. Heavy mineral assemblages and UPb detrital zircon geochronology of sediments from the Weihe and Sanmen Basins: New insights into the Pliocene-Pleistocene evolution of the Yellow River. Palaeogeogr. Palaeoclimatol. Palaeoecol. 562, 110072.
Zhang, H., Nie, J., Liu, X., Pullen, A., Li, G., Peng, W., Zhang, H., 2021b. Spatially variable provenance of the Chinese Loess Plateau. Geology 49.
Zhang, H., Lu, H., He, J., Xie, W., Wang, H., Zhang, H., Breecker, D., Bird, A., Stevens, T., Nie, J., Li, G., 2022. Large-number detrital zircon U-Pb ages reveal global cooling caused the formation of the Chinese Loess Plateau during late Miocene. Sci. Adv. 8 (41), eabq2007.
Zheng, D., Zhang, P.-Z., Wan, J., Yuan, D., Li, C., Yin, G., Zhang, G., Wang, Z., Min, W., Chen, J., 2006. Rapid exhumation at ~8 Ma on the Liupan Shan thrust fault from apatite fission-track thermochronology: Implications for growth of the northeastern Tibetan Plateau margin. Earth Planet. Sci. Lett. 248, 198–208.
Zhou, P., Shi, Z., Li, X., Zhou, W., 2020. Response of Westerly Jet over the Northern Hemisphere to astronomical insolation during the Holocene. Front. Earth Sci. 8, 282.
Zhu, Y., Zhou, L., Mo, D., Kaakinen, A., Zhang, Z., Fortelius, M., 2008. A new magnetostratigraphic framework for late Neogene Hipparion Red Clay in the eastern Loess Plateau of China. Palaeogeogr. Palaeoclimatol. Palaeoecol. 268, 47–57.